Dalton Transactions

Accepted Manuscript

Volume 45 | Number 1 | 7 January 2016 | Pages 1–398

Dalton Transactions

An international journal of inorganic chemistry
www.rsc.org/dalton

ISSN 1477-9226

PAPER
Joseph T. Hupp, Omar K. Farha et al.
Efficient extraction of sulfate from water using a Zr-metal–organic framework

175 YEARS

ROYAL SOCIETY OF CHEMISTRY

rsc.li/dalton

Journal Name

ARTICLE

Highly Porous Palladium Nanodendrites: Wet-chemical Synthesis, Electron Tomography and Catalytic Activity

Stefanos Mourdikoudis,[a,b,c] Verónica Montes-García,[a] Sergio Rodal-Cedeira,[a] Naomi Winckelmans,[d] Ignacio Pérez-Juste,[a] Han Wu,[e] Sara Bals,[d] Jorge Pérez-Juste,[a]* and Isabel Pastoriza-Santos[a]*

A simple procedure to obtain highly porous hydrophilic palladium nanodendrites in one-step is described. The synthetic strategy is based on the thermal reduction of a Pd precursor in the presence of a positively charged polyelectrolyte such as polyethylenimine (PEI). Advanced electron microscopy techniques combined with X-ray diffraction (XRD), thermogravimety and BET analysis demonstrate the polycrystalline nature of the nanodendrites as well as their high porosity and active surface area, facilitating a better understanding of their unique morphology. Besides, catalytic studies performed using Raman scattering and UV-Vis spectroscopies revealed that the nanodendrites exhibit a superior performance as recyclable catalysts towards hydrogenation reaction compared to other noble metal nanoparticles.

Introduction

Metals are one of the most important catalytic systems for chemical transformation.[1, 2] Petroleum refining, fuel cells, and production of chemical intermediates, pharmaceuticals and agrochemicals are some examples of using metals as catalysts. As most of the catalytic reactions occur on metal surfaces, metals at nanometer scale are preferred due to their high surface/volume ratio. Over the years, lots of studies have been focused on the improvement of the catalytic activity of metallic nanoparticles.[3-5] The dominant factors that may affect the catalytic efficiency can be divided into four categories: composition, size and morphology of the nanoparticles and nature of the active sites. The development of different nanotechnology areas has contributed to the fast advance in the fabrication of nanoparticles (monometallic, alloys and hybrids) with full control over their properties. In the field of catalysis, Pd, Au, Pt, Ru and Ag nanoparticles (NPs) have been already extensively exploited, achieving good performance in a large variety of organic transformations.[1, 6-8] Although nanoparticles with smaller dimensions possess a higher number of surface atoms, they do not always show the best performance.[9] For example, Zhu *et al.* found that among 4, 6, 8, and 10 nm Au NPs, 8 nm Au NPs with 4 nm crystallite diameter exhibited the highest catalytic activity for CO_2 reduction to CO.[9] This catalytic effect was explained, based on DFT calculations, due to the presence of an optimum ratio of edge sites that favours the adsorption of reaction intermediates.

Non-spherical nanoparticles are enclosed by a certain number of facets and presenting edges (the intersection of facets) and corners, the intersection of two edges. The edges and corners are constituted by atoms of low-coordination number; therefore those sites have larger surface energies. It is generally accepted that nanoparticles with low coordinated surface atoms show a higher catalytic activity than those with a higher coordination number. Consequently, it is important to optimize not only the size of the nanoparticle to obtain a high surface area but also the number of low-coordination sites (such as edges and corners).[10, 11] Alternatively, metal nanoparticles with high index facets, meaning a set of Miller indices {hkl} with at least one index greater than 1, present a high density of terraces, steps and kinks (constituted as well by low-coordination sites).[12, 13] These high index facets can serve as intrinsically more active sites for catalysis.[14] For example, single-crystal surfaces of bulk Pt possessing high index planes exhibit higher catalytic activity than other single-crystal surfaces with more stable, low-index planes like {111} and {100}.[15] So far most of the metal nanoparticle catalysts reported presents a solid core. But from a structural point of view a porous particle will lead to an increase in the surface area, in comparison with a solid one, due to the presence of an internal surface in addition to the external surface. Furthermore, such configuration could produce an increase in the surface atoms with a low coordination number in comparison to that for a solid structure, leading generally to an improved catalytic activity.[10] For instance, dendritic-like nanoparticles which consist of highly branched arm-composed structure, and therefore can be considered as porous particles, potentially exhibit high catalytic activity thanks to their high surface area and to the presence of low coordinated sites in high densities on their branches.[16-20] In summary, both parameters, that

a. Department of Physical Chemistry and Biomedical Research Center (CINBIO), Universidade de Vigo, 36310 Vigo, Spain. E-mail: juste@uvigo.es, pastoriza@uvigo.es
b. Biophysics Group, Department of Physics and Astronomy, University College London, London, WC1E 6BT, UK.
c. UCL Healthcare Biomagnetic and Nanomaterials Laboratories, 21 Albemarle Street, London W1S 4BS, UK.
d. EMAT-University of Antwerp, Groenenborgerlaan 171, B-2020 Antwerp, Belgium.
e. Centre for Nature Inspired Engineering (CNIE), Department of Chemical Engineering, University College London, Torrington Place, London, WC1E 7JE, UK

Dalton Transactions Accepted Manuscript
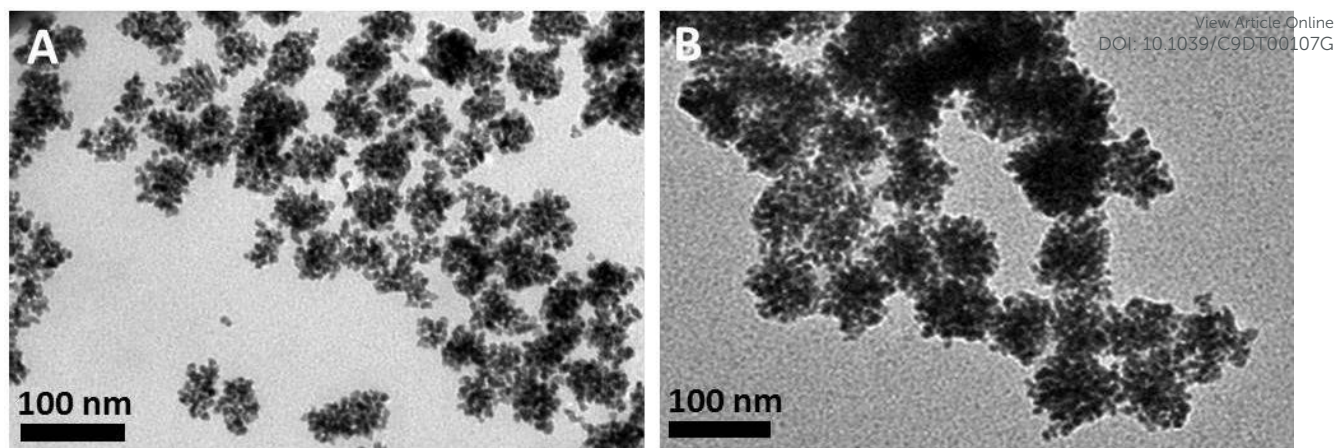
Figure 1. Representative TEM images of PdND1 (A) and PdND2 (B).

is, surface area and density of low-coordination sites are strongly intertwined, and unless the particle shape and crystallinity is perfectly defined both should be taken into consideration at the same time.

In this work, we In this work, we present a one-pot wet chemical strategy to fabricate hydrophilic and highly porous Pd nanodendrites, based on the thermolytic reduction of palladium salts in a high boiling point solvent, such as N, N-dimethylformamide (DMF) or diethylene glycol (DEG), in the presence of polyethylenimine (PEI). Two types of Pd nanodendrites with different porosity and surface area were obtained. The obtained nanodendrites have been analysed by a number of techniques such as high resolution angle annular dark field scanning transmission electron microscopy (HAADF-STEM), 3D tomography, X-ray diffraction (XRD), thermogravimetry and BET analysis in order to obtain information about their morphology, crystallinity as well as the porous structure. Furthermore, we have performed a detailed study of their catalytic activity based on the hydrogenation of 4-nitrophenol (4-NP) to 4-aminophenol (4-AP). Interestingly, we have demonstrated that the reaction process could be followed by Raman spectroscopy which allowed to monitor the reaction on a preparative scale demonstrating the applicability of our catalytic platform in synthetically useful procedures. The results illustrate that the reported Pd nanodendrites present a higher catalytic performance towards hydrogenation reactions compared to other noble metal nanoparticles, such as, Pt, Ag or Au. Additionally, the recyclability tests after several cycles reveal no loss in catalytic activity.

Results and discussion

Pd nanocrystals synthesis and characterization. Two different types of Pd nanodendrites were fabricated using a one-pot wet chemical method. The methodology developed is based on our previous experience on the synthesis of platinum nanodendrites and nanoflowers related to the use of polymers and high boiling point solvents which allows to apply a wide range of synthesis temperatures, thus modifying their reducing capacity.[16, 21] In the present case we studied the reduction of palladium acetylacetonate ($Pd(acac)_2$) or potassium tetrachloropalladate (K_2PdCl_4) in DMF or DEG, respectively, at 150 ºC in the presence of a positively charged polyelectrolyte, such as PEI (see experimental section for details). While the combination of $Pd(acac)_2$ and DMF led to Pd nanodendrites, hereafter PdND$_1$, with an average diameter of 37.4 ± 5.3 nm (see representative TEM images in Figure 1A and Figure S1 in the Supporting information), the reduction of K_2PdCl_4 in DEG resulted in larger nanodendrites (51.8 ± 7.5 nm), PdND$_2$, with an apparently more compact structure (see Figure 1B and Figure S2 in the SI). Moreover, the ζ-potential analysis shows highly positive ζ-potentials for both samples (47.0 ± 0.8 mV for PdND$_1$ and 54.9 ± 0.9 mV for PdND$_2$) indicating the presence of PEI as capping ligand at the nanoparticle surface.

In order to perform a 3D structural analysis, the Pd nanodendrites were characterized by electron tomography based on high angle annular dark field scanning transmission electron microscopy (HAADF-STEM), revealing interconnected arms branching in various orientations for both samples. Figures 2A-B show high resolution HAADF-STEM images of PdND$_1$ (Figure 2A) and PdND$_2$ (Figure 2B) and their corresponding 3D surface visualizations (in yellow). At first sight it can be observed that the dendritic morphology in the PdND$_2$ sample is larger in size and more compact compared to those in the PdND$_1$ sample, which are smaller and more porous. Supporting information videos, SV1 and SV2, show a movie of the 3D reconstructions of both type of particles. The 3D reconstructions were performed using the Discrete Algebraic Reconstruction Technique (DART) as implemented in the ASTRA toolbox.[22-24] Using this technique, segmentation is performed during the reconstruction and as a result, the so-called missing wedge artefacts that limit the amount of information obtainable from the object are significantly reduced in the reconstruction, yielding more reliable quantitative results.[25] Thus the segmented volume can be used to estimate the

active surface area and the porosity. For this purpose, a part in the middle of the reconstructed volume was considered, an example is provided at Figure 2C. This segmented volume contains two different types of voxels: those that belong to Pd and empty voxels or pores. The surface area of the dendrite was calculated as well as the volume of the dendrite and the pores. The porosity is defined as:

$$porosity = \frac{pore}{pore + dendrite}$$

This procedure was repeated for different volumes for the same dendrites. Electron tomography was performed on five different nanodendrites for each type of nanodendrites (see Table S1 in the SI for a detailed description of the porosity and surface area measured for each of the analyzed particles). Table 1 shows the average porosity and surface area measured for $PdND_1$ and $PdNPD_2$. The difference in porosity between the nanodendrites is also reflected by the active surface area values estimated per gram of Pd (Table 1). Thus, an active surface area per gram of ca. 3.7 times and ca. 5.3 times larger for $PdND_1$ and $PdND_2$, respectively, than their corresponding spherical and compact (solid) counterparts is derived (see Table 1 and SI for a detailed description of the surface area estimation). Further insights on the surface area of the samples at a macroscopic level were acquired through thermogravimetric analysis (TGA) and BET analysis. The TGA analysis (Figure S3) reveals a clear

difference in weight loss between both samples (35% and 10% at 600 ºC for $PdND_1$ and $PdND_2$, respectively) suggesting the presence of a higher amount of PEI electrolyte at the first type of dendrites. The different porosities obtained by electron tomography were also reflected by their corresponding pore volume and surface area values obtained by BET (see Table 1 and Figures S4 and S5). Thus, $PdND_1$ present a higher pore volume than $PdND_2$ (0.096 vs 0.067 cm^3 g^{-1}). Additionally, the BET measurements yielded surface area values of 35.3 m^2 g^{-1} and 17.3 m^2 g^{-1} for $PdND_1$ and $PdND_2$, respectively. The higher BET-surface area for $PdND_1$ than $PdND_2$ is in agreement with what one would expect for a material with higher porosity and pore volume. In fact, the considerably lower BET-surface area for $PdND_2$ in comparison to its electron tomography-calculated surface area may be attributed to the following reasons: in BET analysis, the N_2 sorption technique requires the accessibility of the pores/surfaces that allows transport of the gas molecules; therefore the results can only be interpreted to the accessible pores and surfaces. This can be in principle different from the TEM analysis when closed (inaccessible) pores can also be identified. For BET, mesopores (2<d<50 nm) can account for much of the surface measured by this technique. Also BET won't be able to include macropores during measuring. Finally, BET, despite its limitations, is a macroscopic technique, running using around 100 mg of powder of each sample. This includes a vast number of nanodendrites. Electron tomoraphy,
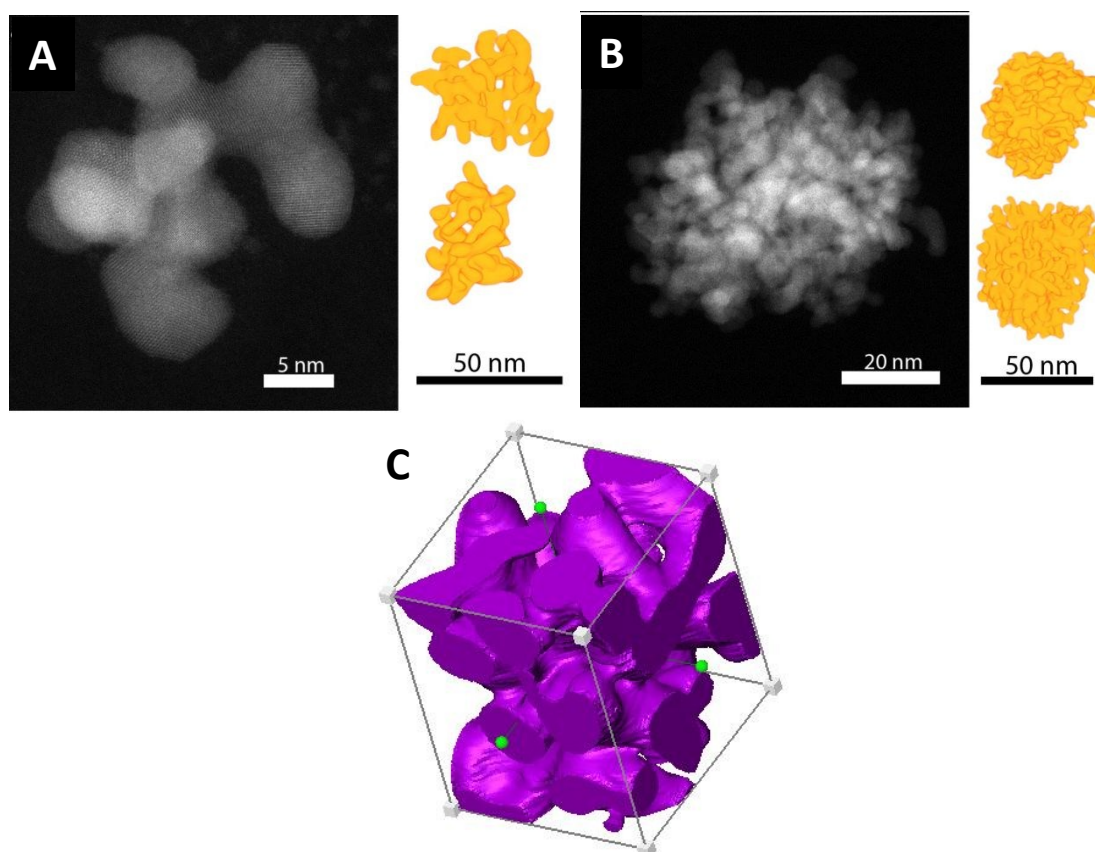
Figure 2. Representative high resolution HAADF-STEM images of $PdND_1$ (A) and $PdND_2$ (B). On the right side in yellow: 3D visualization of the tomographic reconstruction along different viewing directions of the two types of Pd nanodendrites. See supporting information videos for animated versions. (C) Representative 3D visualisation of a central part of the tomographic reconstructed volume used for the calculation of the active surface area and the porosity (see text for details).
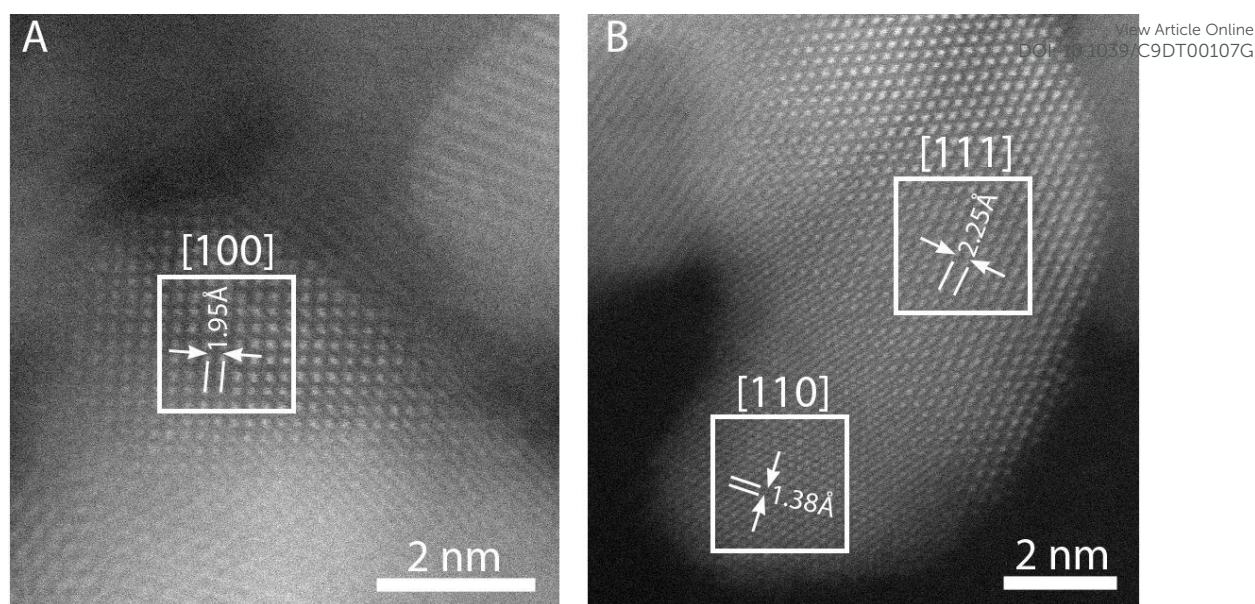
Figure 3. High resolution HAADF-STEM images showing the branches of different Pd nanodendrites oriented along [100] (A) and [110] and [111] (B) directions.

being precise in certain aspects, is a microscopic technique, thus limited in a small number of individual dendrites.

By inspecting the dendrites at the atomic scale, it can be observed that their branches are oriented along multiple crystallographic directions, thus reflecting some degree of polycrystallinity (Figure 3). However, by analyzing different particles it was observed that there is a preferential orientation of the branches along the [111] direction. Furthermore, from the images in Figure 3, the face centered cubic (*fcc*) crystal structure of Pd can be confirmed. Additional crystallographic data were obtained by XRD measurements (Figure S6). XRD patterns recorded for the two samples show characteristic peaks which can be assigned to the [111], [200], [220], [311], and [222] reflections of the *fcc* structure of metallic Pd (JCPDS card #05-0681). The relative intensities between the different peaks are similar to those reported for bulk *fcc* Pd due to the random orientations of the Pd nanoparticles on the supporting substrate.[27] Moreover, the 'macroscopic' XRD screening of the different palladium nanocrystals indicates an abundance of {111} planes in accordance with the high resolution HAADF-STEM analysis of the PdNDs. The mean crystalline grain size of the Pd samples was calculated using the Scherrer's formula [28] from the peak width at

half-maximum using the (111) peak in all cases. The obtained values were 7.8 nm and 4.8 nm for $PdND_1$ and $PdND_2$, respectively. These values are much smaller than those derived by TEM, which implies that the Pd nanocrystals are composed of multiple crystallographic domains, in accordance with the high resolution HAADF-STEM observations (Figure 3A-B). All peaks depicted at the XRD measurements were found to shift by ~ 0.5° toward lower angles as compared to bulk Pd. This indicates that the Pd-Pd interatomic distance increases after formation of the Pd nanocrystals (a sign of lattice expansion), which is in agreement with previous reports.[29]

Regarding the formation mechanism of Pd NDs, such morphology indicates a kinetically controlled process where factors such as solvent, capping agent, temperature and Pd precursor may play critical roles. In our case, the quick appearance of black color during synthesis evidences that the rate at which the newly formed metal atoms are supplied is relatively high. After the formation of the Pd nuclei at initial stage of reaction, the high reduction rate of the Pd precursor might favour that the adatoms deposited on a specific region of the Pd surface (often the most active site) do not migrate to sites with lower free energy but they remain where deposition occurs. This situation could explain the dendritic particle growth.[16,]

Table 1. Average porosities and surface areas obtained by electron tomography and pore volumes and surface areas determined by BET for $PdND_1$ and $PdND_2$.

	Size (nm)[a]	Porosity (%)[b]	Active Surface Area (nm²)[b]	Active Surface Area (m² g⁻¹)	Pore Volume (BET) (cm³/g)	Surface Area (BET) (m² g⁻¹)
$PdND_1$	37.4 ± 5.3	49.4 ± 6.6	8354 ± 1915	50.1[c]/13.3[d]	0.096	35.3
$PdND_2$	51.8 ± 7.5	39.4 ± 4.0	26826 ± 4566	50.6[c]/9.6[d]	0.067	17.3

[a] Particle diameter estimated assuming a spherical geometry. [b] Average values obtained from analysing five different particles for each type of nanodendrite.[c] Estimated surface area per gram of Pd nanodendrites, calculated as explained in Ref. [26] [d] Estimated surface area assuming a spherical geometry and a solid particle.

ARTICLE
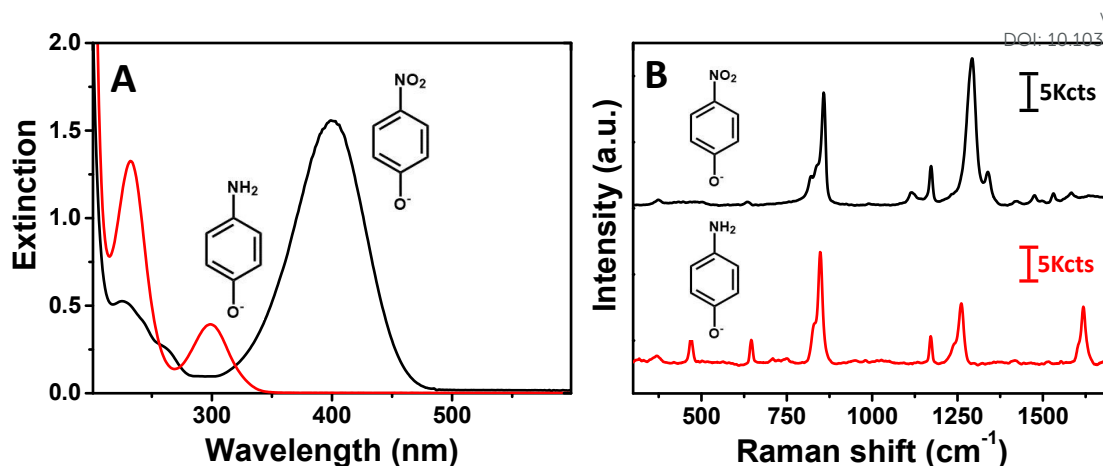
Figure 4. (A) UV-Vis and (B) Raman scattering spectra in liquid state of 4-NP⁻ (black line) and 4-AP⁻ (red line) at pH 11. Raman scattering spectra were collected with a 532 nm laser line, 15X objective, 24.5 mW and 10 s for 4-NP (10^{-2} M) or 30 s for 4-AP⁻ (0.1 M).

[30, 31] Unfortunately, although both approaches give rise to nanodendrites with well-defined size and different porosity, all efforts to control both parameters through systematic variation of parameters such as metal precursor and concentration, surfactant concentration or temperature, among others, were not sucessful. It resulted in either very compact/aggregated structures or more porous structures with very polydisperse, inhomogeneous sizes and shapes. Thus, we restricted oursellves to the study of the catalytic performance of these two types of particles and then we compared with results found in the literature for other catalysts.

Catalytic performance of Pd nanocrystals. The catalytic performance of both kinds of Pd nanodendrites was studied for the hydrogenation of 4-NP to 4-AP by sodium borohydride. It is well known that 4-NP constitutes an especially harmful component of industrial wastewater, on the other hand 4-AP is very useful and important in many applications including analgesic and antipyretic drugs, photographic developers, corrosion inhibitors, among others.[32, 33] Thus, the development of a cost effective, stable, and highly efficient catalyst for the reduction of nitro-compounds to amino-compounds under mild environments is greatly desirable.

Prior to the catalytic studies we have performed the characterization of 4-NP and 4-AP by UV-Vis and Raman scattering spectroscopies (see Figure 4 and Figures S7 and S8 in the SI). First we analyzed the influence of the pH on the absorption and Raman scattering spectrum of 4-NP. As shown in Figure S7A, while at pH 5 the molecule presents the main absorption band at 320 nm, at basic pH a more intense band at 400 nm is observed corresponding to the formation of 4-nitrophenolate (4-NP⁻). In the case of the Raman scattering spectrum of 4-NP (Figure S7B), it⁻ is mainly dominated by ONO bending (858 cm⁻¹) and asymmetric CCH bending (1116, 1172, 1292 and 1339 cm⁻¹) signal.[34] Besides it should be pointed out that a change in pH from 5 to 11 principally led to an inversion of the bands located at 1292 and 1339 cm⁻¹ (see Figure S7B) as well as to increase of most of the Raman signals. Assignment of the observed Raman bands was performed on the basis of DFT calculations (see experimental section and Figure S8 and Table S2 in the SI).

All the catalytic studies were performed at pH 11-12 for two main reasons; first, to enhance the stability of sodium borohydride avoiding its hydrolysis and formation of hydrogen as by-product. The second reason has to do with the fact that the Raman and absorption cross sections of 4-NP⁻ are higher than those for the 4-NP form.

Similarly, 4-AP at basic pH evolves to 4-aminophenolate (4-AP⁻) displaying an absorption band centered at 300 nm (see Figure 4A). Besides, the measured Raman scattering spectrum of 4-AP⁻ is mainly dominated by ring deformation (469 cm⁻¹), ring twisting deformation (645 cm⁻¹), ring breathing (848 cm⁻¹), NH_2 wagging (848 cm⁻¹), NH_2 twisting (1172 cm⁻¹), ring deformation and CCH bending (1261 cm⁻¹) and C=O stretching and CCH bending (rocking) (1619 cm⁻¹) (see Figure 4B). A detailed description of the vibrational assignments of 4-AP⁻ can be found in the Supporting Information, Figure S8 and Table S3.

In summary, both the reactant (4-NP⁻) and the product (4-AP⁻) can be easily distinguished by either UV-Vis or Raman scattering spectroscopy. In order to evaluate the applicability of Raman scattering spectroscopy to study the kinetics of the 4-NP⁻ hydrogenation we have estimated the detection limits of 4-NP⁻ and 4-AP⁻ which are dependent on their corresponding Raman scattering cross section . As shown in Figure S9 in the SI, the limit of detection for 4-NP is 10^{-4} M displays a good linear correlation between the Raman intensity and its concentration in the 10^{-2} M to 10^{-4} M range. On the other hand, the estimated Raman cross section of 4-AP⁻ is significantly lower since its limit of detection is only 5 mM. Thus, the kinetics of the 4-NP⁻ to 4-AP⁻ reduction can be easily followed by Raman spectroscopy by simply monitoring the decrease in the characteristic bands of 4-NP⁻.
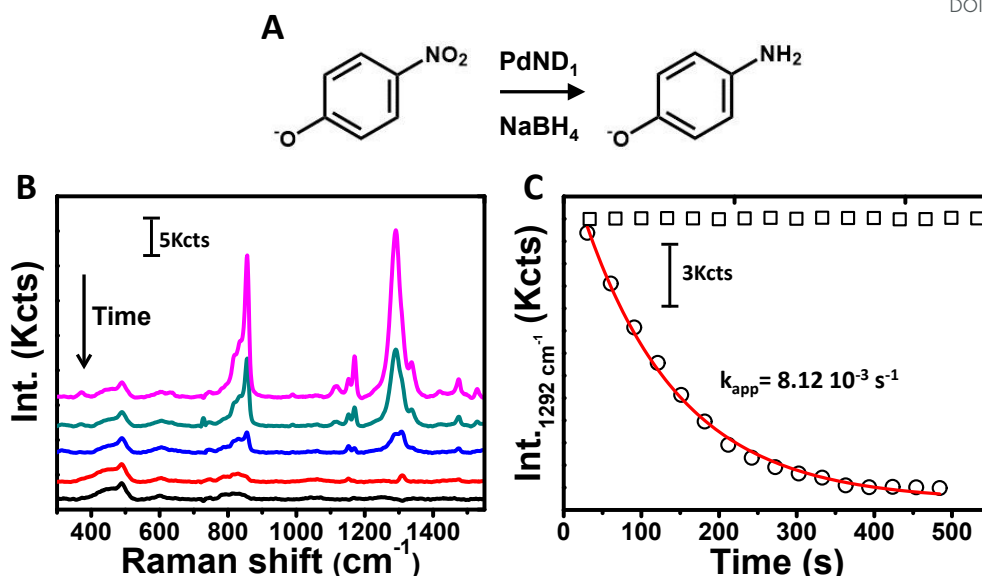
Figure 4. (A) Schematic representation of 4-NP$^-$ reduction to 4-AP$^-$, (B) Spectral evolution of a mixture of 4-NP$^-$ and PdND$_2$ upon borohydride addition. [4-NP$^-$]= 8.2 mM, 0.13 mg of PdND$_2$, [NaBH$_4$]= 77 mM and [NaOH]= 10 mM , T= 25 °C using Raman scattering spectroscopy. (C) Kinetic trace of the Raman intensity at 1292 cm^{-1} during the reduction of 4-NP$^-$ by NaBH$_4$ in the presence (open circles) and in the absence (open squares) of PdND$_2$, the red line represents the best fit to a first order rate constant.

Although sodium borohydride is regarded as a strong reducing agent, it can be considered as inert for the 4-nitrophenol reduction in the absence of a metal catalyst (see Figure 5C). The addition of Pd nanodendrites to the reaction medium led to gradual decrease of the characteristic 4-NP$^-$ Raman bands (see Figure 5B and S10A for PdND$_2$ and PdND$_1$, respectively), indicating the catalytic conversion from 4-NP$^-$ to 4-AP$^-$. The kinetic trace of the reaction is illustrated in Figure 4C (PdND$_2$) and Figure S10B (PdND$_1$) in the SI, where the Raman intensity of the asymmetric CCH bending at 1292 cm^{-1} is represented versus reaction time. Thus a rapid decrease of the Raman intensity is observed until the complete reactant disappearance after 15 or 10

min for PdND$_1$ and PdND$_2$, respectively. It should be noted that a large excess of NaBH$_4$ with respect to 4-NP$^-$ was used (molar ratio of NaBH$_4$ to 4-NP$^-$ of 7:1) and it can be assumed to be constant during the whole reaction and allows us to treat the kinetics of the catalytic process as a pseudo-first order reaction. Therefore, the overall reaction rate can be written as

$$-\frac{d[4NP]}{dt} = k_{obs}\, S\, [NaBH_4][4NP^-] \qquad (1)$$

where k_{obs} is the observed pseudo-first order rate constant, S is the metal catalyst surface, [4-NP$^-$] is the concentration of 4-NP$^-$ at a given time t and [NaBH$_4$] is the sodium borohydride concentration. It can be simplified to

$$-\frac{d[4NP]}{dt} = k_{app}\, [4NP^-] \qquad (2)$$

where k_{app} is the apparent first-order rate constant of the reaction.

Figure 4C and S10B show the fit of the kinetic trace to a first-order rate equation (see the experimental section), which yields an observed rate constant of 3.95×10^{-3} s^{-1} for PdND$_1$ and 8.12×10^{-3} s^{-1} for PdND$_2$.

Under the Raman experimental conditions used and considering the low Raman cross section of 4-AP$^-$ the main peak of 4-AP$^-$ (1262 cm^{-1}, ring deformation and CCH bending) produced during the reaction kinetics was hardly distinguished. Alternatively, once the reaction finished, the Raman spectrum was refined by increasing the acquisition time (60 s) and number of accumulations (10), in such a way that the characteristic 4-AP$^-$ showed up. Figure 5 shows the Raman spectra of commercially available 4-NP$^-$ and 4-AP$^-$ and the corresponding Raman spectra of the reaction mixture at time 0 and 1500 s. The good agreement between the different spectra reveals that all 4-NP$^-$ has been converted into 4-AP$^-$ since none of the
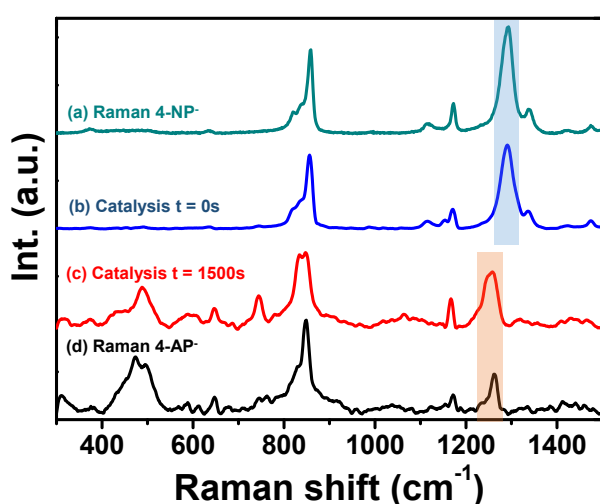
Figure 5. Raman scattering spectra of commercial 4-NP- (a), catalytic reaction at t= 0 (b) and t= 1500 s (c) and commercial 4-AP- (d).

characteristic signals of 4-NP⁻ is present in the spectrum recorded at the end of the reaction.

As pointed out previously the *in situ* Raman measurements allowed us to follow the kinetics of the reaction on a preparative scale. We have also compared the obtained results with a most common and standardized methodology, such as UV-Vis spectroscopy. Under our synthetic conditions the progress of the reaction cannot be followed by UV-Vis spectroscopy due to the high absorption cross section of 4-NP⁻. Alternatively, different aliquots of the reaction mixture (20 µL) were diluted in 400 µL of Milli-Q water to quench the reaction and to allow to measure the UV-Vis spectra. The full reduction of 4-NP⁻ by $NaBH_4$ was completed within 20 min since the complete disappearance of 4-NP⁻ absorption band at 400 nm was observed. Such a process can also be visually appreciated by the gradual change of the originally yellow-green color solution to a colorless one. Figure S11 in the SI shows the UV-Vis time-resolved spectra of the reaction where the absorption band at 400 nm decreases while two new bands at 230 nm and 300 nm characteristics of 4-AP⁻ appear. Similarly to the Raman measurements the experimental conditions allows us to treat the kinetics of the catalytic process as a pseudo-first order reaction (see experimental section), which yields an observed rate constant in agreement to that determined by Raman spectroscopy (see Figures S10 and S11 in the SI).

In order to compare the catalytic activity of the Pd nanodendrites with previous reports, the normalized rate constant (k_{nor}) was determined, which was obtained by normalizing k_{app} with respect to the total amount of catalyst (m) and also the borohydride concentration ($[NaBH_4]$),

$$k_{nor} = {k_{app}}/{(m\,[NaBH_4])} \qquad (3)$$

In the present case the metallic Pd content was determined by ICP-OES spectroscopy to be 0.04 mg and 0.13 mg for $PdND_1$ and $PdND_2$, respectively. Thus, the k_{nor} value obtained for $PdND_1$ and $PdND_2$ is 1274.4 and 787.5 $g^{-1}\,s^{-1}\,M^{-1}$, respectively. This value is greater than the k_{nor} estimated for other nanoparticle-based catalysts, such as Pd black (23 $g^{-1}\,s^{-1}\,M^{-1}$), Pt nanoflowers (233.3 $g^{-1}\,s^{-1}\,M^{-1}$),[30] Pt black (69 $g^{-1}\,s^{-1}\,M^{-1}$),[31] Au@citrate (27.6 $g^{-1}\,s^{-1}\,M^{-1}$)[31] or Ag (68.9 $g^{-1}\,s^{-1}\,M^{-1}$)[32] and Au (77.5 $g^{-1}\,s^{-1}\,M^{-1}$)[33] dendrites (see Table S4 in the SI), indicating their superior performance. Interestingly, it should be pointed out that between the two different types of Pd nanodendrites presented here, the smaller ones ($PdND_1$) show a catalytic activity that is 1.62-fold times higher than the more compact nanodendrites ($PdND_2$). Such increase in catalytic activity could be attributed to its higher degree of porosity and BET-surface area as well as to the presence of more surface defects and kinks.

To test the recyclability of the Pd nanodendrites as catalysts, the nitro to amine conversion was repeated several times using the same colloidal dispersion, through the sequential addition of 4-NP⁻ to an aqueous solution containing excess sodium borohydride and a constant concentration of the catalyst. Figure 6 and Figure S12 in the SI show the plot of the Raman intensity at 1292 cm^{-1} vs. reaction time for $PdND_2$ and $PdND_1$, respectively, as well as a fit to a first-order rate equation for each 4-NP⁻ addition. As it can be seen from the plots, the first-order kinetic behavior was perfectly reproducible in both cases, as predicted by equation 2. The catalyst reusability with a yield of 100% 4-NP⁻ hydrogenation indicated no loss in catalytic activity for

both types of palladium nanodendrites. Moreover, the consistency of the calculated apparent rate constant, k_{app}, alongside the different additions/cycles (5 in total) of 4-NP⁻ ($8.12 \times 10^{-3}\,s^{-1}$, $9.93 \times 10^{-3}\,s^{-1}$, $8.01 \times 10^{-3}\,s^{-1}$, $7.35 \times 10^{-3}\,s^{-1}$ and $6.52 \times 10^{-3}\,s^{-1}$ for $PdND_2$, see Figure 7) and ($2.13 \times 10^{-3}\,s^{-1}$, $3.95 \times 10^{-3}\,s^{-1}$, $3.69 \times 10^{-3}\,s^{-1}$, $3.30 \times 10^{-3}\,s^{-1}$ and $3.95 \times 10^{-3}\,s^{-1}$ for $PdND_1$, see Figure S10 in the SI) is a clear evidence for the remarkable stability of the $PdND_x$ in the reaction medium, as well as the reproducibility of their catalytic activity. Commonly, the deactivation of catalytic efficiency during reusability of colloidal catalysts, has been attributed to the aggregation of the metal nanoparticles causing a decrease in the active catalytic surface area [37]. In our case, the high catalytic reusability can be ascribed to the high stability provided by the positively charged polymer PEI even at high ionic strength. The $PdND_1$ nanoparticles were observed by TEM after the catalytic cycles and, as shown in Figure S13 in the SI the reduction of 4-NP⁻ did not affect the dendritic morphology. Additionally, in order to check the reusability of the particles in terms of recovery we analysed the catalytic activity after several centrifugation and redispersion cycles (see Figure 6B and experimental section for details). It can be observed that although the conversion was complete, there is a slight decrease in the efficiency, in terms of rate constant, with the different cycles which can be attributed most likely to nanoparticle loss during the washing cycles rather surface poisoning since the addition of more reactant did not lead to a decrease in the observed rate constant (see Figure 6A).
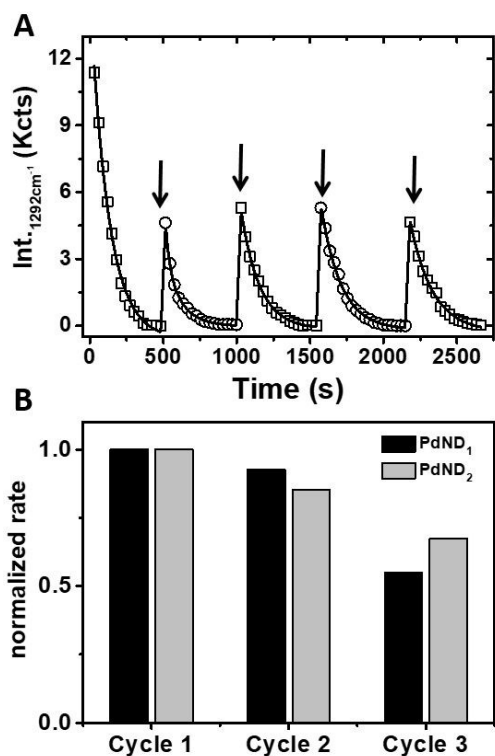
Figure 6. (A) Raman kinetic traces at 1292 cm^{-1}, registered during the sequential reduction of 4-AP^{-} using PdND$_2$ as catalyst. The arrows indicate the times at which 4-NP^{-} was added to obtain [4-NP^{-}]= 2.75 mM and [NaOH]= 10 mM. The line represents the best fit to a first-order rate equation in each cycle. (B) Reusability test of both type of Pd nanoparticles upon centrifugation and redispersion cycles.

Conclusions

In summary, highly porous multi-crystalline Pd nanodendrites with a relatively narrow size distribution have been synthesized through a one-step procedure via the thermally assisted reduction of palladium salt precursors in the presence of PEI as surfactant. The nanoparticles were readily dispersed into water after synthesis and washing stages. HAADF-STEM and electron tomography analysis allowed to discern their particular three-dimensional morphology revealing a high degree of porosity and active surface area. The obtained Pd nanodendrites present a higher catalytic performance towards hydrogenation reactions compared to other noble metal nanoparticles, such as, Pt, Ag or Au. Finally, the recyclability tests after several cycles reveal no loss in catalytic activity.

Conflicts of interest

There are no conflicts to declare.

Experimental

Materials.

Dimethylformamide (DMF, >98%), branched polyethyleneimine (PEI, Mw~ 25000), palladium (II) acetylacetonate (Pd(acac)$_2$, 99%), potassium tetrachloropalladate (K$_2$PdCl$_4$, 99.99%), oleylamine (OAm, 70% - technical grade), sodium hydroxide (NaOH, ≥97.0%, pellets),

sodium borohydride (NaBH$_4$, 99%) were purchased from Sigma-Aldrich. Diethylene glycol (DEG, 99.98%) was provided from Fischer Sci. 4-aminophenol (4-AP, 98%) was supported by Alfa Aesar. 4-nitrophenol was purchased from Fluka. Pure grade ethanol, acetone and Milli-Q water were used as solvents. All glassware was rigorously cleaned in *aqua regia* before use.

Synthesis of Pd nanocrystals. The palladium nanocrystals utilized in this work were prepared as follows:

a) Pd nanodendrites, PdND$_1$, were prepared as follows: 860 mg of PEI were introduced in a three-neck flask containing 30 ml of DMF under stirring. After 20-min stay at room temperature, the mixture was heated up to 130 ^{o}C. At this point, 0.1 mmol of solid Pd(acac)$_2$ were rapidly added in the above solution. The reaction mixture turned black at once, indicating the formation of nanoparticles. The flask was then heated to 150 ^{o}C for 1 h in air. After cooling to room temperature, the product was precipitated with excess ethanol, and washed three times with ethanol, acetone and water successively (8500 rpm, 15 min). The nanodendrites were finally dispersed into deionized water (30 mL).

b) Pd nanodendrites, PdND$_2$, were synthesized with the next protocol: in a three-neck flask and under magnetic stirring conditions, 15 ml of DEG and 15 ml of OAm were inserted followed by the addition of 860 mg of PEI. The mixture was stirred for 20 min at room temperature. Afterwards, 0.3 mmol of K$_2$PdCl$_4$ were introduced. The resulting mixture was further stirred for a few minutes, before being rapidly heated (~12 ^{o}C/min) to 150 ^{o}C for 1 h, in air. The product was then left to cool naturally at room temperature. Precipitation and washing steps were carried out similarly to the case of the PDND$_1$. The final product was stored in water, 30 mL.

Characterization of Pd nanocrystals. Conventional TEM images were recorded using a JEOL JEM 1010 microscope operating at an acceleration voltage of 100 kV. Electron tomography experiments were carried out using a Tecnai G2 Electron Microscope, operated at 200 kV. All tilt series were acquired in HAADF-STEM mode, in order to avoid any unwanted diffraction contrast. For the acquisition, a Fischione model 2020 single tomography holder was used and the series were acquired over a tilt range from -76° to +76° and using an increment of 2°. Tomographic reconstructions were performed using the Discrete Algebraic Reconstruction Technique (DART) as implemented in ASTRA toolbox.[22, 23] Using this technique, segmentation is performed during the reconstruction and as a result, the so-called "missing wedge artefacts" are significantly reduced in the reconstruction, yielding more reliable quantitative results[25] High resolution HAADF-STEM images of the particles were acquired using a double aberration corrected cubed FEI Titan 50-80 electron microscope operated at 300 kV. XRD powder measurements were carried out after drying some quantities of the colloidal solutions of the samples. A Siemens D-5000 diffractometer with a CuKα radiation (1.54059 Å) was used for these measurements. FTIR spectra were recorded using a Nicolet 6700 FTIR spectrometer with a resolution of 4 cm^{-1} using previously dried powder of palladium nanocrystals. The surface charge (reflected in ζ-potentials) of Pd nanocrystals was evaluated through electrophoretic mobility measurements by taking the average of five measurements at the stationary level, using a

Journal Name

ARTICLE

Malvern Zetasizer 2000 instrument (Worcestershire, U.K.), equipped with a 4 mW helium-neon laser (633 nm) as a source of incident light and operating at a scattering angle of 17° and 25 °C. Diluted aqueous solutions of Pd nanocrystals were injected in disposable ζ cells and successively inserted in the apparatus. The obtained data were analysed using the software provided with the instrument. Thermogravimetric analyses were performed using a TG-DSC Setsys evolution 16/18 (Setaram) with a heating ramp rate of 10ºC min^{-1} from 20 to 800 ºC and in a nitrogen flow. The surface feature and pore structure of PdND samples were determined and analysed using adsorption/desorption isotherms of N_2 at 77 K with a QUADRASORB evo (Quantachrome Instrument, Florida, USA). Prior to the N_2 sorption measurements, the samples were outgassed at 383 K under high vacuum for 20 h. The specific surface area of PdNd samples was calculated using multi-point BET (Brunauer, Emmett and Teller) analysis from the adsorption isotherm. The pore size distributions were obtained using the BJH model from the desorption isotherm. Finally, ICP-OES elemental analyses were performed after digestion of the samples with aqua regia.

4-Nitrophenol to 4-aminophenol reduction. In a 1 cm length path quartz cuvette, 2 mL of an aqueous solution containing 10 mM of 4-NP (10mM in NaOH) were mixed with 0.25 mL of an aqueous dispersion of PdND$_x$ containing either 0.04 mg of PdND$_1$ or 0.13 mg of PdND$_2$, followed by the addition 0.188 mL of a freshly prepared NaBH$_4$ solution 0.1 M. Raman experiments were conducted with a Renishaw InVia Reflex confocal system. The spectrograph used a high-resolution grating (1800 grooves per mm) with additional band-pass filter optics, a confocal microscope, and a 2D-CCD camera. Excitation was carried out at 532 nm with a laser power at the sample of 25 mW. Raman characterization of the hydrogenation reaction was done using a macrosampler accessory to measure in liquid state. The catalytic reaction was monitored by the decrease with time of the 4-NP main signal (1292 cm^{-1}, ring deformation). For the hydrogenation reaction subsequent spectra were taken with one accumulation and an acquisition time of 30 seconds per spectra. For the last spectra of the catalysis, in order to detect the 4-AP, ten accumulation and an acquisition time of 60 seconds were used. The apparent observed rate constants k$_{app}$ were calculated from the plots of Raman intensity of 4-NP$^-$ (1292 cm^{-1}) vs. time, using the first-order rate equation:

$$I_t = I_f + \Delta I\ e^{-kt} \tag{4}$$

where I$_t$ is the Raman intensity of 4-NP$^-$ at time t, I$_f$ is the final Raman intensity of 4-NP$^-$ and k is the apparent observed first-order rate constant of the reaction.

A diode-array UV-Vis spectrophotometer (Agilent 8453) was employed to monitor the reaction by recording absorbance spectra every 60 s, at room temperature. The 4-aminophenol product was identified by monitoring the changes with time of the absorbance at 400 nm, where the maximum variations take place. To measure variations of absorbance we had to make dilutions of sample (20 μL in 400 μL) and we recorded spectra using a 1mm quartz cuvette. The apparent observed rate constants k$_{app}$ were calculated in an analogous way to the plots of absorbance vs. time but using absorbance vs. time instead of Raman intensity of 4-NP (1292 cm^{-1}) (equation 4).

Recyclability test. When the catalytic reduction of 4-NP to 4-AP was deemed completed, 0.1mL of 4-NP (70mM) was added again to the reaction solution, and the kinetic studies were continued after mixing. This procedure was repeated several times.

Computational methods. Geometrical optimization of the structures of 4NP- and 4AP- were carried out employing density functional theory (DFT) at the M062X/6-311++G** level, followed by analysis of their vibrational frequencies to characterize the structures obtained as energy minima. All computations were performed using Gaussian09.[34] Assignment of the theoretical Raman spectrum to molecular vibrational modes was performed by visual inspection of the atomic displacements for each vibrational mode in combination with the results from the VEDA program, which generates an optimized set of internal coordinates based on the molecular structure and provides a potential energy distribution for the quantitative analysis of vibrational spectra.[35]

Acknowledgements

Notes and references

1. P. Herves, M. Perez-Lorenzo, L. M. Liz-Marzan, J. Dzubiella, Y. Lu and M. Ballauff, *Chem. Soc. Rev.*, 2012, **41**, 5577-5587.
2. L. He, F. Weniger, H. Neumann and M. Beller, *Angew. Chem. Int. Ed.*, 2016, **55**, 12582-12594.
3. Z.-P. Liu and P. Hu, *J. Amer. Chem. Soc.*, 2003, **125**, 1958-1967.
4. S. Chong and T. C.-K. Yang, *Materials*, 2017, **10**, 756.
5. S. Mourdikoudis, M. Chirea, D. Zanaga, T. Altantzis, M. Mitrakas, S. Bals, L. M. Liz-Marzan, J. Perez-Juste and I. Pastoriza-Santos, *Nanoscale*, 2015, **7**, 8739-8747.
6. D. Wang and D. Astruc, *Chem. Soc. Rev.*, 2017, **46**, 816-854.
7. P. Taladriz-Blanco, P. Herves and J. Perez-Juste, *Top. Catal.*, 2013, **56**, 1154-1170.
8. G. C. Zheng, K. Kaefer, S. Mourdikoudis, L. Polavarapu, B. Vaz, S. E. Cartmell, A. Bouleghlimat, N. J. Buurma, L. Yate, A. R. de Lera, L. M. Liz-Marzan, I. Pastoriza-Santos and J. Perez-Juste, *J Phys Chem Lett*, 2015, **6**, 230-238.
9. W. Zhu, R. Michalsky, Ö. Metin, H. Lv, S. Guo, C. J. Wright, X. Sun, A. A. Peterson and S. Sun, *J. Amer. Chem. Soc.*, 2013, **135**, 16833-16836.
10. L. M. Falicov and G. A. Somorjai, *Proc. Natl. Acad. Sci. U.S.A*, 1985, **82**, 2207-2211.
11. B. Ni and X. Wang, *Adv. Sci.*, 2015, **2**, 1500085.

12. Y. Xia, Y. Xiong, B. Lim and S. E. Skrabalak, *Angew. Chem. Int. Ed.*, 2009, **48**, 60-103.

13. S. Rodal-Cedeira, V. Montes-Garcia, L. Polavarapu, D. M. Solis, H. Heidari, A. La Porta, M. Angiola, A. Martucci, J. M. Taboada, F. Obelleiro, S. Bals, J. Perez-Juste and I. Pastoriza-Santos, *Chem. Mater.*, 2016, **28**, 9169-9180.

14. Q. F. Zhang and H. Wang, *ACS Catal.*, 2014, **4**, 4027-4033.

15. R. Huang, Y.-H. Wen, Z.-Z. Zhu and S.-G. Sun, *J. Mater. Chem.*, 2011, **21**, 11578-11584.

16. S. Mourdikoudis, M. Chirea, T. Altantzis, I. Pastoriza-Santos, J. Perez-Juste, F. Silva, S. Bals and L. M. Liz-Marzan, *Nanoscale*, 2013, **5**, 4776-4784.

17. M. Sanles-Sobrido, M. A. Correa-Duarte, S. Carregal-Romero, B. Rodríguez-González, R. A. Álvarez-Puebla, P. Hervés and L. M. Liz-Marzán, *Chem. Mater.*, 2009, **21**, 1531-1535.

18. Y.-H. Chen, H.-H. Hung and M. H. Huang, *J. Amer. Chem. Soc.*, 2009, **131**, 9114-9121.

19. P. Kannan, J. Dolinska, T. Maiyalagan and M. Opallo, *Nanoscale*, 2014, **6**, 11169-11176.

20. Q. Gao, M. R. Gao, J. W. Liu, M. Y. Chen, C. H. Cui, H. H. Li and S. H. Yu, *Nanoscale*, 2013, **5**, 3202-3207.

21. S. Mourdikoudis, T. Altantzis, L. M. Liz-Marzán, S. Bals, I. Pastoriza-Santos and J. Pérez-Juste, *Crystengcomm*, 2016, **18**, 3422-3427.

22. K. J. Batenburg, S. Bals, J. Sijbers, C. Kubel, P. A. Midgley, J. C. Hernandez, U. Kaiser, E. R. Encina, E. A. Coronado and G. Van Tendeloo, *Ultramicroscopy*, 2009, **109**, 730-740.

23. W. J. Palenstijn, K. J. Batenburg and J. Sijbers, *J Struct Biol*, 2011, **176**, 250-253.

24. W. J. Palenstijn, K. J. Batenburg and J. Sijbers, 13th International Conference on Computational and Mathematical Methods in Science and Engineering, Almería (Spain), 2013.

25. E. Biermans, L. Molina, K. J. Batenburg, S. Bals and G. Van Tendeloo, *Nano Lett*, 2010, **10**, 5014-5019.

26. J. Ustarroz, B. Geboes, H. Vanrompay, K. Sentosun, S. Bals, T. Breugelmans and A. Hubin, *Acs Appl Mater Inter*, 2017, **9**, 16168-16177.

27. G. Berhault, M. Bausach, L. Bisson, L. Becerra, C. Thomazeau and D. Uzio, *J. Phys. Chem. C*, 2007, **111**, 5915-5925.

28. B. Cullity, *2nd ed.; Addison-Wesley: Reading, MA*, 1978, 102.

29. S. Yang, J. Dong, Z. Yao, C. Shen, X. Shi, Y. Tian, S. Lin and X. Zhang, *Sci. Rep.*, 2014, **4**, 4501.

30. Y. W. Lee, M. Kim, Y. Kim, S. W. Kang, J.-H. Lee and S. W. Han, *J. Phys. Chem. C*, 2010, **114**, 7689-7693.

31. Y. Wook Lee, M. Kim and S. Woo Han, *Chem. Comm.*, 2010, **46**, 1535-1537.

32. M. J. Vaidya, S. M. Kulkarni and R. V. Chaudhari, *Org. Process Res. Dev.*, 2003, **7**, 202-208.

33. Z. D. Pozun, S. E. Rodenbusch, E. Keller, K. Tran, W. Tang, K. J. Stevenson and G. Henkelman, *J. Phys. Chem. C*, 2013, **117**, 7598-7604.

34. M. Muniz-Miranda, *Appl. Catal. B*, 2014, **146**, 147-150.

35. J.-J. Lv, A.-J. Wang, X. Ma, R.-Y. Xiang, J.-R. Chen and J.-J. Feng, *J. Mater. Chem. A*, 2015, **3**, 290-296.

36. W. Ye, Y. Chen, F. Zhou, C. Wang and Y. Li, *J. Mater. Chem.*, 2012, **22**, 18327-18334.

37. Y. Qiu, Z. Ma and P. Hu, *J. Mater. Chem. A*, 2014, **2**, 13471-13478.

38. M. J. Frisch, G. W. Trucks, H. B. Schlegel, G. E. Scuseria, M. A. Robb, J. R. Cheeseman, G. Scalmani, V. Barone, B. Mennucci, G. A. Petersson and J. E. Peralta, *Gaussian 09, Revision D.01,*, Wallingford CT, 2009.

39. M. H. Jamroz, *Spectrochim. Acta A*, 2013, **114**, 220-230.